Digital Suppression of Transmitter Leakage in FDD RF Transceivers: Aliasing Elimination and Model Selection

Wenhui Cao, *Student Member, IEEE,* Yue Li, *Student Member, IEEE,* and Anding Zhu, *Senior Member, IEEE*

***Abstract*—The transmitter (TX) induced interference due to power amplifier (PA) nonlinearities poses severe desensitization problems to the receiver (RX) chain in frequency-division duplexing (FDD) transceivers. Due to nonlinear signal process involved, a high sampling rate is normally required in the existing digital suppression approaches, which can result in high cost and high power consumption in wideband systems. In this paper, a new digital suppression model is proposed to cancel the TX leakage at baseband with a low sampling rate. The cancellation model is based on the modified decomposed vector rotation (DVR) model. With the addition of cross-term products, the enhanced model is capable of eliminating the aliasing effect arising from the reduced sampling rate. Theoretical analysis of aliasing elimination is presented, and the algorithm is subsequently verified by both simulation and experiment results, confirming the effectiveness and feasibility of the proposed cancellation technique for TX leakage suppression. Compared to conventional solutions, the new approach uses much less hardware resource and consumes much lower power while achieving comparable performance.**

***Index Terms*—Aliasing effect, aliasing elimination, behavioral model, cross terms, frequency-division duplexing (FDD), leakage suppression, low sampling rate, transceiver.**

I. Introduction

In frequency-division duplexing (FDD) transceivers, transmitter (TX) and receiver (RX) share the same antenna but operate at different frequency bands. With increasing demands for high data rates and wider signal bandwidths, the choices of frequency band allocations for TX and RX become limited in the new generation wireless systems. As a consequence, spacings between the TX and RX carriers can vary significantly, either being very wide or very narrow. This creates significant challenges for transceiver design, especially in carrier aggregation where multiple bands may be deployed at the same time. Due to nonlinear behavior of the TX, in particular, the nonlinearity induced by RF power amplifiers (PAs), inter-modulation products of the TX signal can cause interference to the RX operated at the adjacent frequency band, as shown in Fig. 1. To eliminate the interference, bandpass filtering in the duplexer is normally conducted to isolate the TX and RX paths. However, in the case of narrow separation, duplexer filter may fail to block the interference induced by the TX. For instance, in LTE standard [1], e.g., Band 31, the carrier frequency separation between TX and RX can be as narrow as 10 MHz. When the PA operates at a high output power level, the interference induced by the PA nonlinearities in the TX path can be quite strong and thus is very likely to contaminate the received signal.

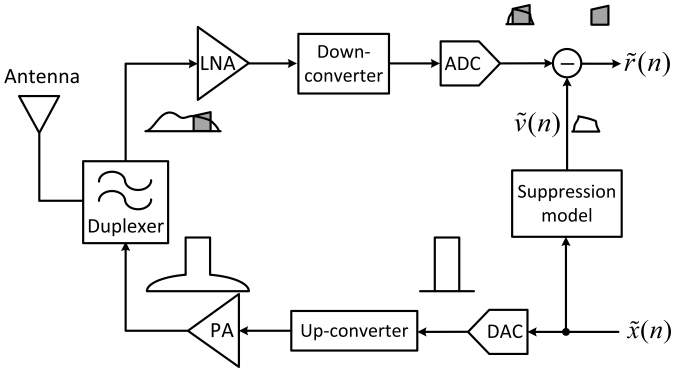

Fig. 1. TX-induced interference at the receiver band in FDD transceivers.

In the literature, various suppression strategies have been proposed to resolve the transmitter leakage issue. Some researchers proposed digital suppression for out-of-band (OOB) distortion at the transmitter chain based on digital predistortion [2]–[7]. The other approaches are to insert compensation modules into the RX chain [8]–[18], subtracting the TX-induced inference to restore the signal fidelity. Among these approaches, direct digital suppression has become a preferable choice because of its flexibility and easy implementation. This approach "directly" map the *baseband* input to a *baseband*-equivalent representation of OOB emission by using a nonlinear behavioral model. The estimated replica can then be subtracted from the received signal to restore the integrity of the desired signal, as shown in Fig. 1. Due to a nonlinear process involved, the sampling rate must be set high enough during the signal generation to avoid aliasing effect. For instance, in [9], a sampling rate at 12 times input signal bandwidth was used. In [17], the signal was sampled with a sampling rate of 13 times input bandwidth. With increasing demands for higher data rates, the signal bandwidth in wireless systems will continue to increase. Processing a signal with a sampling rate of multiple times the input signal bandwidth will require very high speed digital circuits that not only increases implementation cost but

This work was funded by Science Foundation Ireland under Grant Numbers 12/IA/1267 and 13/RC/2077.

W. Cao is with the Institute of Antennas and Microwave Technology, School of Electronics and Information, Hangzhou Dianzi University, Hangzhou, 310018, China and she was with the School of Electrical and Electronic Engineering, University College Dublin, Dublin 4, Ireland (e-mail: wenhui.cao@ucdconnect.ie).

Y. Li and A. Zhu are with the School of Electrical and Electronic Engineering, University College Dublin, Dublin 4, Ireland (e-mail: yue.li1@ucdconnect.ie; anding.zhu@ucd.ie).

more importantly significantly increases power consumption of the system due to high clock rates.

In this paper, we propose to use low sampling rate data to generate the desired sideband replica. After theoretical analysis, we find that the aliasing effect arising from the reduced sampling rate can be eliminated by introducing cross-term products in the behavioral model. The simulation and experiment results confirm that low sampling rate operation can achieve comparable sideband suppression performance as the full sampling rate solution in FDD transceivers but uses much less hardware resource and consumes much lower power. The rest of the paper is organized as follows: detailed analysis of aliasing effect at low sampling rate case is presented in section II; Section III explains why the cross-terms products are essential for aliasing elimination; the simulation results are given in Section IV and the experimental results and hardware complexity comparison are reported in Section V with a conclusion in Section VI.

II. Aliasing Effect in Sideband Replica Generation

A. The Reference Signal

The principle of digital suppression is that the TX leakage is subtracted from the received signal in the RX so that the originally received signal can be restored. To do so, we need to know the targeted reference signal, i.e., the OOB emission that falls in the receiver band. This signal can be captured at the receiver output with the receiver antenna turned off, shown in Fig. 2, where the PA output directly goes through the duplexer, low-noise amplifier (LNA), downconverter, and is finally sampled by the analog-to-digital converter (ADC). Although the bandwidth of the PA output can be very wide, we only need to consider the distortion that falls in the receiver band. Therefore, the bandwidth of the targeted cancellation signal is relatively narrow. As long as the sampling rate of the ADC covers the receiver bandwidth, the TX-induced interference is free from aliasing effect.

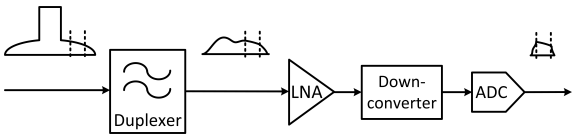

Fig. 2. The reference signal generation.

B. Sideband Replica Generation

After obtaining the reference, the task now is to generate the desired compensation signal, i.e., the sideband replica, from the original input, as shown in Fig. 3(a). This task can be conducted in three steps: frequency shift, nonlinear modeling and band-limiting filtering, as shown in Fig. 3(b) and described in detail below.

Firstly, because the center frequencies of transmit and receive signals are different, a frequency shift on the baseband signal is required. This frequency shift can be conducted before or after nonlinear modeling. Here we shift the frequency

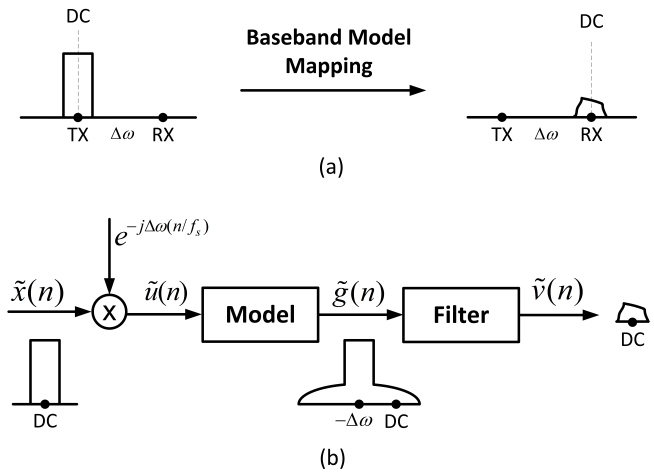

Fig. 3. The sideband replica generation.

before nonlinear modeling. The PA input signal is frequency-shifted by $\Delta\omega$, the TX-RX separation frequency, given by

$$\tilde{u}(n) = \tilde{x}(n)e^{-j\Delta\omega(n/f_s)} \tag{1}$$

where $\tilde{x}(n)$ is the baseband input signal and $\tilde{u}(n)$ represents the frequency-shifted output signal. f_s is the sampling rate of the signal.

Subsequently, the frequency-shifted PA input should go through a nonlinear behavioral model that represents the nonlinear characteristics of the PA. In the literature, Volterra-based behavioral models, such as memory polynomial (MP) [19], generalized memory polynomial (GMP) [20] and dynamic deviation reduction-based (DDR) [21] models, are commonly used. For example, the MP model can be expressed as

$$\tilde{g}(n) = \sum_{i=0}^{M}\sum_{p=0}^{P} c_{i,p}|\tilde{u}(n-i)|^{2p}\tilde{u}(n-i) \tag{2}$$

where $\tilde{g}(n)$ represents the output of PA behavioral model with a set of coefficients $c_{i,p}$. M denotes the memory length and P is the polynomial order. Different from the application in digital predistortion where the model is required to cover the full bandwidth, to fit the sideband distortion, only partial spectrum needs to be covered. The orders of polynomial terms need to be pre-determined to cover the targeted band, and all irrelevant orders shall be discarded. For example, if the leakage location is within 5th-order spectrum, then 3rd-order nonlinear component can be omitted [17].

In the next step, to match the bandwidth of target reference, a band-limiting technique [22] [9] can be employed to filter out the unwanted frequency components in the model output. It is achieved by imposing a band-limiting function, i.e., a finite impulse response (FIR) filter, upon each model operator according to the observation bandwidth of the system. The total suppression model can be expressed as

$$\tilde{v}(n) = \sum_{i=0}^{M}\sum_{p=0}^{P} \tilde{c}_{BL,ip}[G_{i,p}(\tilde{u}(n)) * H] \tag{3}$$

where $\tilde{v}(n)$ is the sideband replica and $G_{i,p}(\tilde{u}(n))$ represent different nonlinear operators in suppression model. $\tilde{c}_{BL,ip}$

are the coefficients of suppression model after band-limiting operation. H represents the impulse response of the FIR filter and $*$ represents the convolution operation.

C. Aliasing Effect

From Fig. 3(a), we can see that both the original input and the desired sideband replica are relatively narrow band, namely, they only occupy the in-band bandwidth of the TX and RX. In principle, a sampling rate of twice the in-band bandwidth would be enough to process these signals. However, due to the nonlinear signal processing required in the signal generation, a much higher sampling rate is needed in order to obtain an aliasing-free replica signal. As illustrated in Fig. 3(a), due to the nonlinear behavior of the PA, the bandwidth of the input signal is expanded multiple times. If a sampling rate with twice the total bandwidth, i.e., $f_s > 2B$, is used and the sideband signal can be generated without aliasing, as shown in Fig. 4(a). However, if the sampling rate is lower than twice of the total bandwidth, i.e., $f_s < 2B$, aliasing will occur, namely, the left and right sides of the spectrum will overlap each other. In this scenario, there are three different cases depending on the sideband locations, shown in Fig. 4(b): (1) Case 1: the sideband is located near the TX center carrier and no overlapping occurs at the sideband; (2) Case 2: the sideband is located in the first Nyquist zone but with overlapping; (3) Case 3: the sideband is located farther away from the TX carrier, placed out of the first-zone of the sampling range. In this case, the sideband signal is folded to the other side of the center frequency, e.g., spectrum slice 3 is folded to 3'. In Case 1, since there is no aliasing at the RX band, the sideband replica can be obtained from the model output by applying a band-limiting filter, while in Case 2 and 3, the aliasing distortion is included in the signal after filtering. This creates an issue that the model output does not match the desired output, shown in Fig. 4(c). This mismatch can significantly degrade the suppression performance. A high sampling rate, therefore, is often used in the existing approaches in the literature.

III. Aliasing Elimination and Model Selection

With continuously increasing demands for higher data rates, the TX and RX signal bandwidths in the wireless systems will continue increase. Processing a signal with a sampling rate of multiple times the signal bandwidth will require very high speed digital circuits that not only increases implementation cost but also significantly increases power consumption of the system. Requiring a high sampling rate in the sideband replica generation is thus not favorable. In this section, we intend to investigate if a lower sampling rate can be employed in the signal generation without introducing significant aliasing effect.

In order to investigate the spectral mismatch problem shown in Fig. 4 (c), we compare the two signal generation processes using a system setup shown in Fig. 5. In the upper branch, the input signal passes the PA, and the sideband filter is then down-sampled by two, while in the lower branch, the input signal is down-sampled by two first and then enters the PA and is filtered by the sideband filter. The upper branch

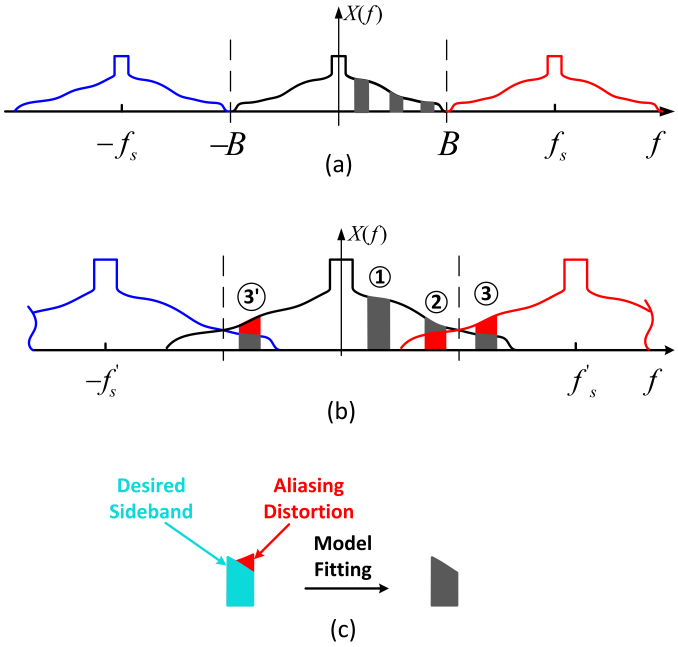

Fig. 4. Aliasing effect demonstration.

represents the model reference signal generation, where no aliasing occurs, while the lower branch represents the sideband replica generation with a lower sampling rate, where the aliasing affects the final signal. To simplify the derivation, a memoryless 5th-order polynomial model is used to represent the PA, given by

$$\tilde{y}(n) = \tilde{b}_1\tilde{x}(n) + \tilde{b}_3|\tilde{x}(n)|^2\tilde{x}(n) + \tilde{b}_5|\tilde{x}(n)|^4\tilde{x}(n) \quad (4)$$

where $\tilde{y}(n)$ represents PA model output and $\tilde{b}_i$ are the coefficients. A FIR filter is used for the sideband signal filtering.

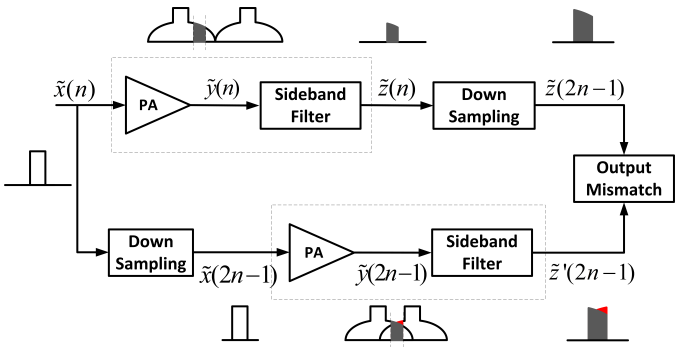

Fig. 5. Mismatch between reference signal generation and sideband replica generation.

A. Model Mismatch

On one side, considering the FIR convolution operation in the upper branch, the filtered sideband signal at high sampling rate can be defined as $[\tilde{z}(1), \tilde{z}(2), \tilde{z}(3), \ldots, \tilde{z}(n)]$, where $\tilde{z}(n)$ is the weighted sum of current and Q past samples, that can be expressed as

$$\tilde{z}(n) = \sum_{q=0}^{Q} \tilde{y}(n-q)h(q) \quad (5)$$

or in a vector format,

$$Z = Y * H \tag{6}$$

where H is the transfer function of the filter with Q delay taps and the vector Y is given by

$$Y = \begin{bmatrix} \tilde{x}(1) & |\tilde{x}(1)|^2\tilde{x}(1) & |\tilde{x}(1)|^4\tilde{x}(1) \\ \tilde{x}(2) & |\tilde{x}(2)|^2\tilde{x}(2) & |\tilde{x}(2)|^4\tilde{x}(2) \\ \vdots & \vdots & \vdots \\ \tilde{x}(n) & |\tilde{x}(n)|^2\tilde{x}(n) & |\tilde{x}(n)|^4\tilde{x}(n) \\ \vdots & \vdots & \vdots \end{bmatrix} \begin{bmatrix} \tilde{b}_1 \\ \tilde{b}_3 \\ \tilde{b}_5. \end{bmatrix} \tag{7}$$

Assuming the high speed TX leakage signal is down-sampled by a factor of 2, the output vector is described as $[\tilde{z}(1), \tilde{z}(3), \ldots, \tilde{z}(2n-1)]$, where $\tilde{z}(2n-1)$ can be stated as

$$\begin{aligned} \tilde{z}(2n-1) = \sum_{q=0}^{Q} [&\tilde{b}_1\tilde{x}(2n-1-q) \\ &+ \tilde{b}_3|\tilde{x}(2n-1-q)|^2\tilde{x}(2n-1-q) \\ &+ \tilde{b}_5|\tilde{x}(2n-1-q)|^4\tilde{x}(2n-1-q)]h(q). \end{aligned} \tag{8}$$

The output becomes a sum of multiple memory terms with respect to the input sample $\tilde{x}(n)$. It is worth noting that the memory effects introduced here are due to filtering process while the PA is memoryless. Moreover, even though the number of the vector elements is halved after down-sampling, the nonlinear components in each output sample remain the same, which involves high speed input samples, as can be seen from (8).

On the other side, in sideband replica generation, the input signal is down-sampled first before entering the PA. The input vector can be described as $[\tilde{x}(1), \tilde{x}(3), \ldots, \tilde{x}(2n-1)]$. The input goes through the memoryless behavioral model and then a FIR filter. The vector format of the operation can be expressed as

$$Z' = Y' * H' \tag{9}$$

where H' is the transfer function of filter with Q' delay taps at the low sampling rate. Vector Y' is expressed as

$$Y' = \begin{bmatrix} \tilde{x}(1) & |\tilde{x}(1)|^2\tilde{x}(1) & |\tilde{x}(1)|^4\tilde{x}(1) \\ \tilde{x}(3) & |\tilde{x}(3)|^2\tilde{x}(3) & |\tilde{x}(3)|^4\tilde{x}(3) \\ \vdots & \vdots & \vdots \\ \tilde{x}(2n-1) & |\tilde{x}(2n-1)|^2\tilde{x}(2n-1) & |\tilde{x}(2n-1)|^4\tilde{x}(2n-1) \\ \vdots & \vdots & \vdots \end{bmatrix} \begin{bmatrix} \tilde{b}_1 \\ \tilde{b}_3 \\ \tilde{b}_5 \end{bmatrix}. \tag{10}$$

The convolution result $[\tilde{z}'(1), \tilde{z}'(3), \ldots, \tilde{z}'(2n-1)]$ is given by

$$\begin{aligned} \tilde{z}'(2n-1) = \sum_{q=0}^{Q'} [&\tilde{b}_1\tilde{x}(2(n-q)-1) \\ &+ \tilde{b}_3|\tilde{x}(2(n-q)-1)|^2\tilde{x}(2(n-q)-1) \\ &+ \tilde{b}_5|\tilde{x}(2(n-q)-1)|^4\tilde{x}(2(n-q)-1)]h'(q). \end{aligned} \tag{11}$$

If we compare the outputs of the two branches, $\tilde{z}(2n-1)$ (the target) and $\tilde{z}'(2n-1)$ (the modeled), the mismatch can be immediately revealed. For instance, the basis terms for $\tilde{z}(5)$ are listed in Table I while the components associated with $\tilde{z}'(5)$ are listed in Table II.

TABLE I
THE CONSTRUCTING BASIS TERMS OF $\tilde{z}(5)$

Model order	The constructing basis terms of $\tilde{z}(5)$
1^{st} order	$\tilde{x}(1)$, $\tilde{x}(2)$, $\tilde{x}(3)$, $\tilde{x}(4)$, $\tilde{x}(5)$
3^{rd} order	$\|\tilde{x}(1)\|^2\tilde{x}(1)$, $\|\tilde{x}(2)\|^2\tilde{x}(2)$, $\|\tilde{x}(3)\|^2\tilde{x}(3)$, $\|\tilde{x}(4)\|^2\tilde{x}(4)$, $\|\tilde{x}(5)\|^2\tilde{x}(5)$
5^{th} order	$\|\tilde{x}(1)\|^4\tilde{x}(1)$, $\|\tilde{x}(2)\|^4\tilde{x}(2)$, $\|\tilde{x}(3)\|^4\tilde{x}(3)$, $\|\tilde{x}(4)\|^4\tilde{x}(4)$, $\|\tilde{x}(5)\|^4\tilde{x}(5)$

TABLE II
THE CONSTRUCTING BASIS TERMS OF $\tilde{z}'(5)$

Model order	The constructing basis terms of $\tilde{z}'(5)$
1^{st} order	$\tilde{x}(1)$, $\tilde{x}(3)$, $\tilde{x}(5)$
3^{rd} order	$\|\tilde{x}(1)\|^2\tilde{x}(1)$, $\|\tilde{x}(3)\|^2\tilde{x}(3)$, $\|\tilde{x}(5)\|^2\tilde{x}(5)$
5^{th} order	$\|\tilde{x}(1)\|^4\tilde{x}(1)$, $\|\tilde{x}(3)\|^4\tilde{x}(3)$, $\|\tilde{x}(5)\|^4\tilde{x}(5)$

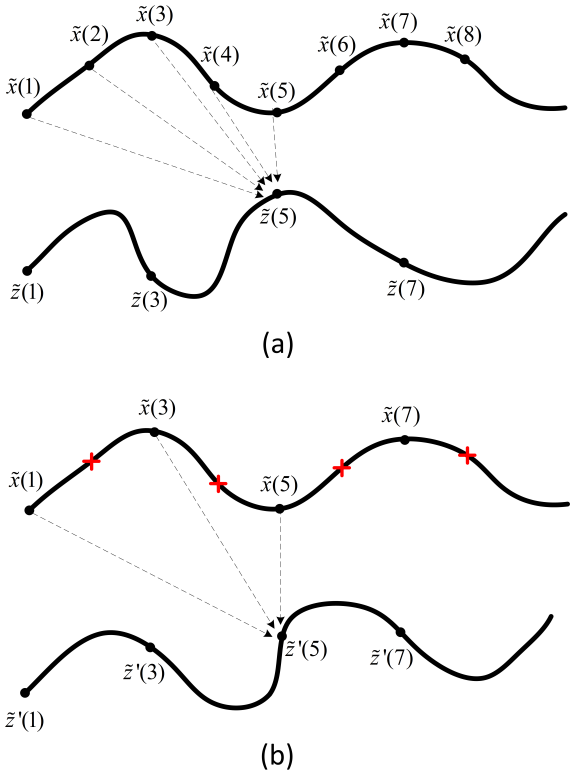

Fig. 6. Input to output mapping

The mismatch can be more clearly illustrated if we compare their input-output relationship. As displayed in Fig. 6(a), $\tilde{z}(5)$ is calculated from samples $\tilde{x}(1)$, $\tilde{x}(2)$, $\tilde{x}(3)$, $\tilde{x}(4)$ and $\tilde{x}(5)$. By contrast, the generation of $\tilde{z}'(5)$ only involves $\tilde{x}(1)$, $\tilde{x}(3)$ and $\tilde{x}(5)$, as shown in Fig. 6(b). Due to the reduction of the sampling rate, the polynomial terms related to $\tilde{x}(2)$ and $\tilde{x}(4)$, e.g., $|\tilde{x}(2)|^2\tilde{x}(2)$, $|\tilde{x}(4)|^2\tilde{x}(4)$, are missing in $\tilde{z}'(5)$. This leads that aliasing effect occurs in the output, which can degrade the suppression performance.

B. Aliasing Elimination Solution

To avoid aliasing or to find the "lost" samples, an obvious solution is to interpolate the input signal to a higher sampling rate but that will significantly increase cost and power assumption in digital circuits as discussed earlier. Here we try to find an alternative solution. The idea is that, instead of directly interpolating the input signal, we recover the "lost" information by using extra modeling terms in the model.

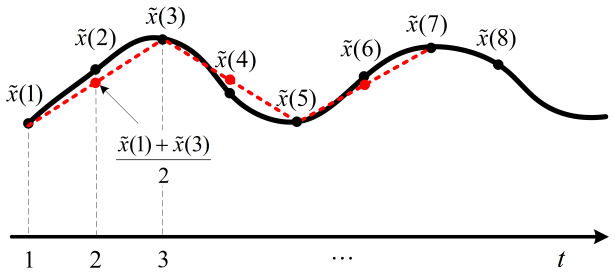

Fig. 7. Interpolation approximation.

In the simplest case, as shown in Fig. 7, $\tilde{x}(2)$ can be approximately expressed as the average of the two adjacent samples $\tilde{x}(1)$ and $\tilde{x}(3)$, written as

$$\tilde{x}(2) = [\tilde{x}(1) + \tilde{x}(3)]/2. \tag{12}$$

The corresponding third-order polynomial term, $|\tilde{x}(2)|^2\tilde{x}(2)$, can then be found as

$$\begin{aligned} &|\tilde{x}(2)|^2\tilde{x}(2) \\ &= \frac{[|\tilde{x}(1)|^2 + |\tilde{x}(3)|^2 + 2\,|\tilde{x}(1)|\,|\tilde{x}(3)|\cos(\theta_1-\theta_3)] \times \tilde{x}(1)}{8} \\ &+ \frac{[|\tilde{x}(1)|^2 + |\tilde{x}(3)|^2 + 2\,|\tilde{x}(1)|\,|\tilde{x}(3)|\cos(\theta_1-\theta_3)] \times \tilde{x}(3)}{8}. \end{aligned} \tag{13}$$

where θ_1 and θ_3 is the phase information of the $\tilde{x}(1)$ and $\tilde{x}(3)$, respectively. The detailed derivations of third-order polynomial term are given in Appendix and the other nonlinear terms can be derived in the same way.

With the above derivation, we can see that the missing nonlinear term, $|\tilde{x}(2)|^2\tilde{x}(2)$, can be represented by a sum of combinations of the existing terms, $\tilde{x}(1)$ and $\tilde{x}(3)$. Among these combinations, $|\tilde{x}(1)|^2\tilde{x}(1)$, $|\tilde{x}(3)|^2\tilde{x}(3)$, are already included in the model, listed in Table II. The rest terms, such as $|\tilde{x}(1)|^2\tilde{x}(3)$, $|\tilde{x}(3)|^2\tilde{x}(1)$, $|\tilde{x}(1)||\tilde{x}(3)|\tilde{x}(3)$, $\cdots$ can be constructed by using cross products. The $cos(\theta_1 - \theta_3)$ can be treated as the weight for the cross-term product, which can be absorbed into model coefficients during the model construction. This means that the missing information in the low sampling rate data can be recovered by using the cross terms in the model. This leads that, to avoid performance degradation due to aliasing effect, we can include cross-term products in the behavioral model instead of interpolating the original input signal during the sideband replica generation. This can avoid the high sampling rate requirement and thus reduce cost and power consumption of digital circuits, as discussed in Section V later.

It is worth mentioning that cross-term products have been used to represent memory effects in PA behavioral models with memory and the final sideband suppression model structures may appear to be similar to those of the existing behavioral models. For instance, $|\tilde{x}(1)|^2\tilde{x}(3)$ may already appear in GMP model. In this work, however, using cross-term products has a special objective, namely, to eliminate aliasing effect. Due to this reason, there are some special requirements for selecting the cross terms. For instance, as shown in Section IV, in a memeryless system, usually there is no need to use cross terms to model memory effects, but in order to eliminate aliasing effect, certain cross terms must be included in the model. In addition, it should be noticed that the above derivation in (13) is only an example to illustrate the feasibility of using cross terms in the model to recover the "missing" information in the low sampling rate signal processing and the recovery is not precise but based on an approximation. A full recovery of the "missing" information or completely eliminating aliasing effect would need a much more sophisticated solution. Nevertheless, this approach provides an alternative solution to the low sampling rate based sideband replica signal generation.

C. Model Selection

In order to integrate the cross-term products in the PA behavioral model, a proper model structure should be selected. As mentioned earlier, conventional methods are deploying the Volterra-based models. In the Volterra models, the bandwidth of the spectrum expansion depends on the order of nonlinear terms chosen. For instance, as shown in Fig. 8(a), the 3rd-term covers three times the original bandwidth while the 5th-order term covers five times the original bandwidth. By using the Volterra-based models, the selection of the nonlinear terms depends on the frequency space between TX and RX, or the location of the desired compensation replica. For instance, if the RX band is located at the fifth order sideband zone, the 3rd-order and lower order terms should be eliminated from the model. This means that if the location of RX is changed, the corresponding nonlinear components in the model should be adjusted. This leads that different model structures must be used in different TX-RX spacings, which can complicate the model construction process. In the wide-spacing case, the order of the nonlinear terms can be very high, which can cause ill-conditioning problems in model extraction [17].

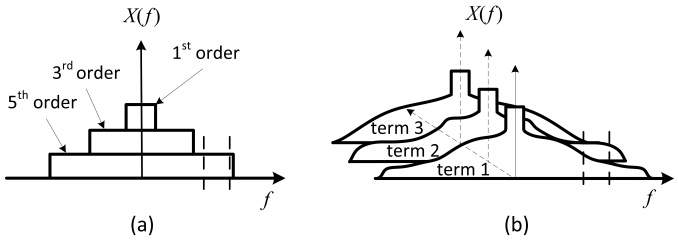

Fig. 8. The comparison of model structures of Volterra model and DVR model.

To avoid these potential issues, a recently proposed behavioral model, named decomposed rotation vector (DVR) [23],

is chosen in this work. The DVR model is given by

$$\begin{aligned}\tilde{y}(n)|_{DVR} = &\sum_{i=0}^{M} \tilde{c}_{i,0}\tilde{x}(n-i) \\ &+ \sum_{k=1}^{K}\sum_{i=0}^{M} \tilde{c}_{ki,1}\,||\tilde{x}(n-i)| - \beta_k|\, e^{j\theta(n-i)} \\ &+ \sum_{k=1}^{K}\sum_{i=0}^{M} \tilde{c}_{ki,21}\,||\tilde{x}(n-i)| - \beta_k|\, e^{j\theta(n-i)} \cdot |\tilde{x}(n)| \\ &+ \cdots\end{aligned} \tag{14}$$

where $\tilde{x}(n)$ and $\tilde{y}(n)|_{DVR}$ represents input and output of DVR model at baseband, respectively. β_k is the threshold value that divides the input range into K partitions. The inner $|\cdot|$ returns magnitude of the input signal, while the outer $|\cdot|$ gives the result of absolute value operation. θ_n represents the phase of $\tilde{x}(n)$. M denotes the memory depth and $\tilde{c}_{ki,j}$ are model parameters, respectively.

Compared to the Volterra-based models, the DVR model is much more flexible in modeling various nonlinearities and every nonlinear term is capable of covering a wide bandwidth in the frequency domain, as shown in Fig. 8(b) [24]. It means that the same structure or terms can be used to generate different sideband replica regardless of the TX-RX spacing. Moreover, the complexity of hardware implementation of the DVR model can also be much lower compared to that of the Volterra-based models [25]. As shown in Table III, various cross-term products in the DVR model can be used to approximate the required cross terms in the replica generation, including third-order and higher order nonlinear terms.

TABLE III
THE APPROXIMATION OF CROSS-TERM PRODUCTS IN DVR MODEL

Cross-term types	Nonlinear approximation in DVR model
$\|\tilde{x}(n-i)\|^2\tilde{x}(n)$ $\|\tilde{x}(n)\|^2\tilde{x}(n-i)$	$\|\|\tilde{x}(n-i)\| - \beta_k\|\,\tilde{x}(n)$ $\|\|\tilde{x}(n)\| - \beta_k\|\,\tilde{x}(n-i)$
$\|\tilde{x}(n-i)\|\|\tilde{x}(n)\|\tilde{x}(n)$ $\|\tilde{x}(n-i)\|\|\tilde{x}(n)\|\tilde{x}(n-i)$	$\|\|\tilde{x}(n-i)\| - \beta_k\|\,e^{j\theta_n}\|\tilde{x}(n-i)\|$ $\|\|\tilde{x}(n-i)\| - \beta_k\|\,e^{j\theta_{n-i}}\|\tilde{x}(n)\|$ $\|\|\tilde{x}(n)\| - \beta_k\|\,e^{j\theta_{n-i}}\|\tilde{x}(n)\|$ $\|\|\tilde{x}(n)\| - \beta_k\|\,e^{j\theta_n}\|\tilde{x}(n-i)\|$
Other nonlinear types	$\|\|\tilde{x}(n-i)\| - \beta_k\|\,e^{j\theta_n}$ $\|\|\tilde{x}(n)\| - \beta_k\|\,e^{j\theta_{n-i}}, \cdots$

IV. SIMULATION RESULTS

To verify the feasibility of the proposed solution, computer simulation was conducted in MATLAB to validate whether adding cross-term products in the model can help eliminate aliasing effect in sideband replica generation. Since cross-term products have been used to represent memory effects in a PA with memory, to avoid confusion, in this simulation, a 11th order memoryless polynomial model was used to represent the nonlinear PA. A complex-valued baseband input with 20 MHz bandwidth was applied to the PA model to generate the output. The signal was then filtered by a band-limiting filter to produce the target 20 MHz leakage reference. The RX-TX frequency space was set as 34 MHz and the sampling rate of the signal was 368.64 mega-samples per second (MSPS).

To avoid using the same PA behavioral model, we employed a memoryless DVR model to construct the desired sideband replica. The number of the threshold value was set to 8. In total, the suppression model required 17 coefficients. Prior to the investigation of the sideband cancellation in low sampling rate scenario, the simulation with a memeryless DVR model at the full sampling rate was conducted and the suppression performance is given in Fig. 9, where we can see that the TX leakage can be effectively removed after compensation. This result proves that the selected DVR model is working properly and the achieved suppression performance serves as a reference for the remaining results.

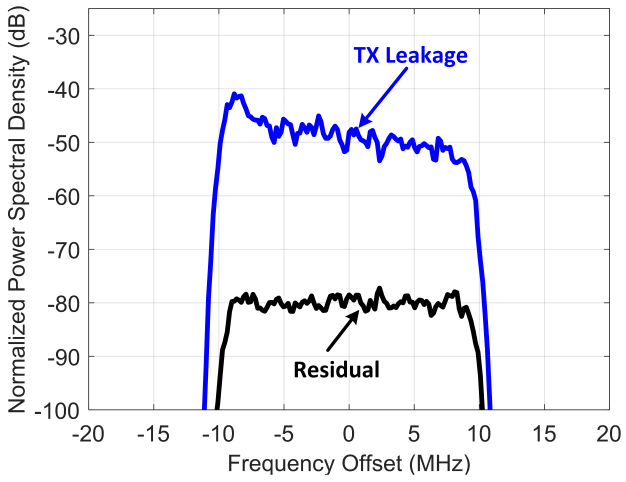

Fig. 9. The simulation result for full-speed rate.

To verify the low-sampling operation, both the input and the reference signal were down-sampled by a factor of 5, with the sampling rate reduced from 368.64 MSPS to 73.72 MSPS. Due to the reduced sampling rate, aliasing effect occurs in the sideband, illustrated in Fig. 10.

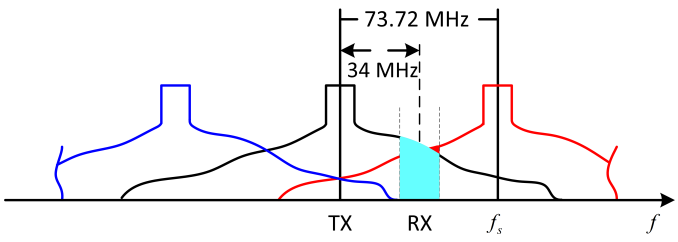

Fig. 10. The demonstration of sideband replica with aliasing effect.

To better verify the theory of aliasing elimination and evaluate the performance of proposed sideband model, the tests were conducted with two types of target signals, as shown in Fig. 11: (1) Match Case: both the model output and the target reference have alias; and (2) Mismatch Case: the model output has alias while the target reference does not have alias. The mismatch case is the actual case in a real system as described earlier in Section II. To create the match case, the high-rate PA output was down-sampled by 5 times (to 73.72 MHz) first, and then going through the low-rate filter.

In this case, aliasing effect occurs in both the modeled and the target signals. In principle, the existing memoryless model should be able to produce the desired sideband compensation signal, meaning that the expected performance of the match case shall be approximately the same as that in full-speed scenario. The spectral comparison of the mismatch and the match cases is shown in the Fig. 12, where we can see a large aliasing distortion is included in the output signal.

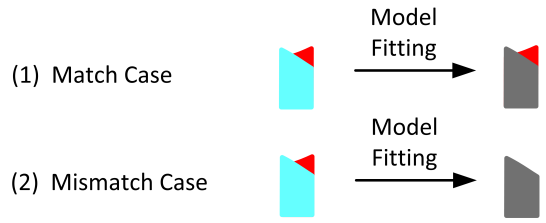

Fig. 11. Model fitting cases.

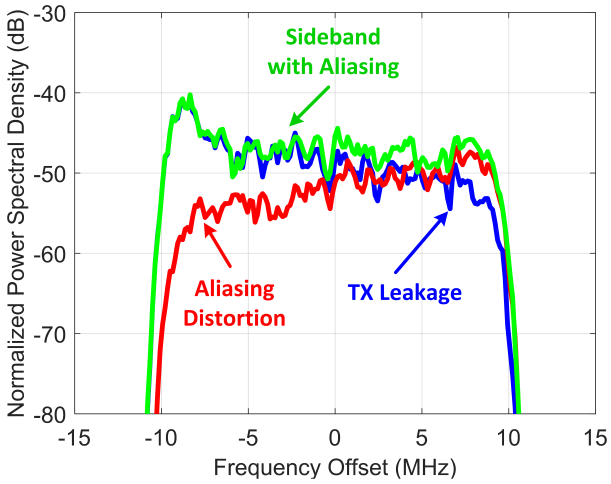

Fig. 12. Spectral comparison of the mismatch and match cases.

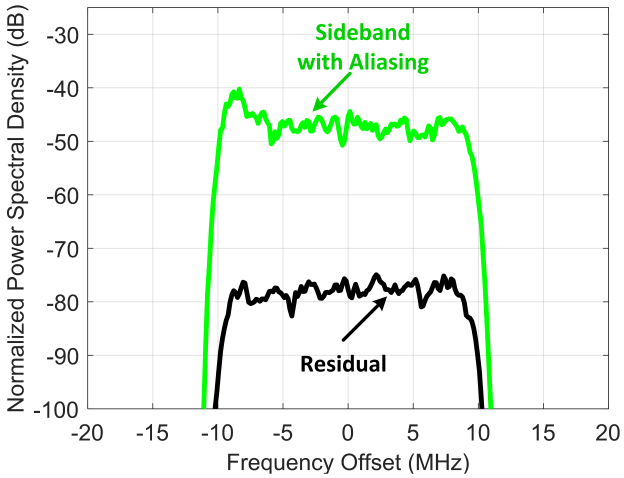

Fig. 13. Suppression result of memoryless DVR model for the match case.

The suppression performance for the two cases is presented in Fig. 13 and Fig. 14, respectively. Simulation result of the match case shows the residual is suppressed to around -78 dBc, which indicates that the DVR model without memory terms can precisely generate the sideband replica in the match case, proving the fitting capability of the DVR model. On the contrary, the same memoryless DVR model cannot track the TX leakage in the mismatch case, the large residual interference in Fig. 14 implies that the memoryless DVR model is incapable of aliasing cancellation.

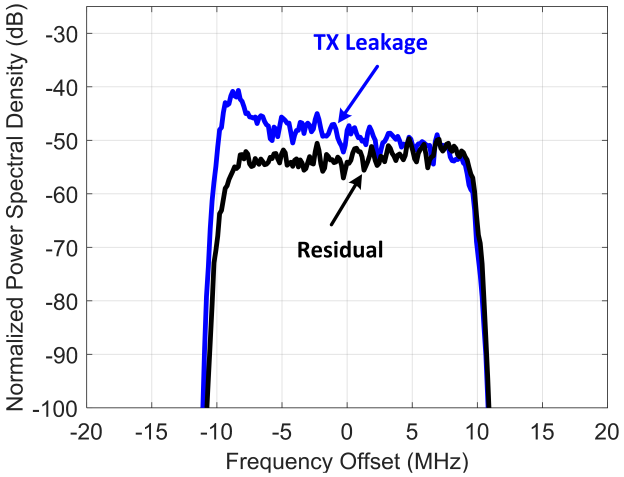

Fig. 14. Suppression result of memoryless DVR model for the mismatch case.

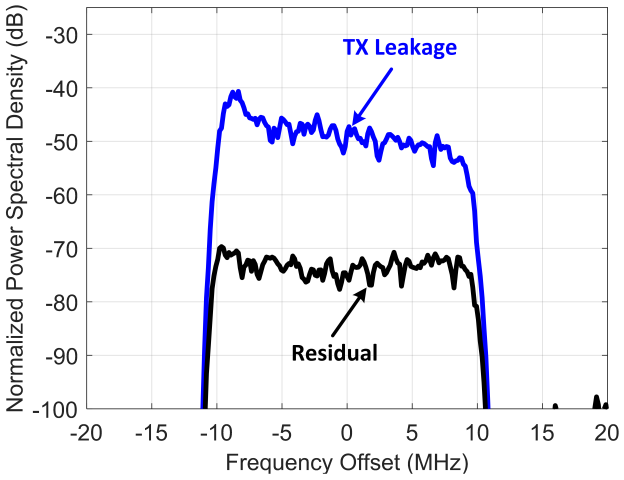

Fig. 15. Simulation result of cross-term products for the mismatch case.

However, this problem can be solved by introducing more cross terms to the memoryless behavioral model. The nonlinear terms listed in Table III were taken into consideration to construct the DVR model. The threshold value was set to 8 and memory length was 4. In total, the number of coefficients was 212. The simulated output is displayed in Fig. 15, where we can see that the aliasing distortion induced by the down-sampling operation can be largely corrected by using cross-term products. Even though the performance is not as good

as that of the full-rate and the match cases, this result proves that introducing cross-term products is an effective solution to eliminating the aliasing effect in low sampling rate signal processing.

V. Experimental Results

To further test the effectiveness of the proposed aliasing elimination approach, experimental measurements are conducted on a real PA on a test bench. The test platform setup includes a PC, a baseband FPGA board, an RF board and a PA, as shown in Fig. 16. The baseband in-phase and quadrature (I/Q) digital signal source was generated from PC. In the TX chain, the baseband signal was modulated and up-converted to RF frequency by the RF board, and finally amplified by the PA. Due to hardware limitation, there was no duplexer used in the platform. Instead of selectively sampling the TX leakage, the RX chain captured the full PA output and sent back to PC, which can be regarded as TX-induced interference with the RX shutdown. The response of the RF front end was assumed to be ideal in this scenario. The time alignment and model extraction were operated off-line in MATLAB.

One concern about the experimental setup is that, due to the limitation of the test bench, the ADC needs to capture the entire output of the PA, where the power and dynamic ranges of the signal are much higher than that of the sideband. It will lead to a reduction in the effective number of bits (ENOBs) distributed to the sideband spectrum, which inevitably deteriorates the signal precision as well as the accuracy of model extraction. However, the main idea of this paper is to verify the theory of aliasing elimination in the low sampling rate scenario, therefore the absolute suppression performance is not the main concern as long as fair comparisons are made between different test scenarios.

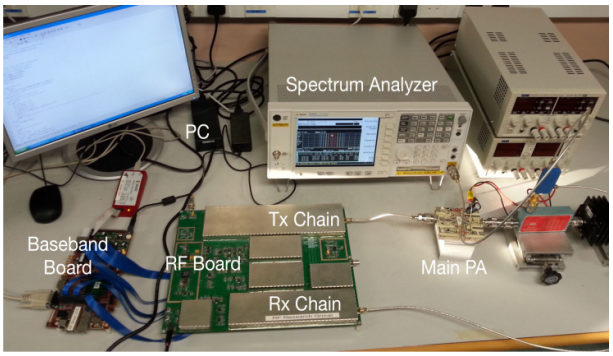

Fig. 16. The experimental test bench.

The PA under test was an in-house designed LDMOS power amplifier operating at 2.14 GHz and excited by an input signal with 20 MHz bandwidth. The PA output spectrum was captured at a high sampling rate of 368.64 MSPS, from which a sideband of 20 MHz bandwidth was filtered as the TX-induced interference. The TX-RX frequency gap was set as 30.72 MHz. To provide a performance reference, the TX leakage suppression at full speed is depicted in Fig. 17. Since the signal was captured from the practical PA platform, memory effect had to be taken into consideration. The full-speed suppression model employed the DVR model structure in [23]. The number of the threshold value K was set 8, memory depth was 3, totally resulting in 43 coefficients.

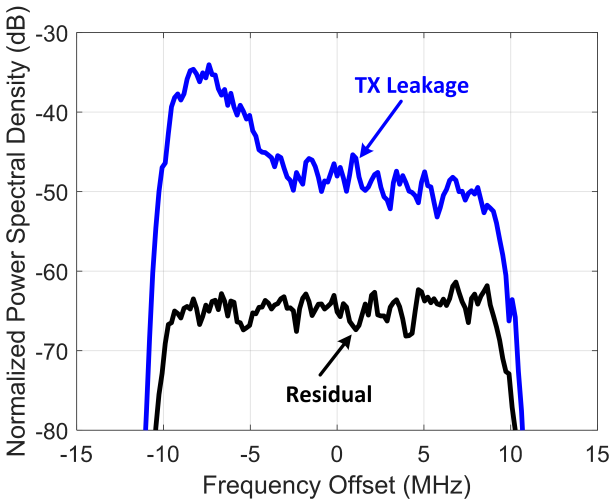

Fig. 17. The suppression reference performance of TX leakage at full speed.

A. Experimental Results for Aliasing Elimination

To test the low-rate scenario, the PA input signal and leakage distortion were down-sampled by 6 times, resulting in a sampling rate of 61.44 MSPS. A low-pass FIR filter was designed to have 20 MHz bandwidth. The spectra of the TX leakage / mismatch case and sideband with aliasing / match case are shown in Fig. 18. Here the aliasing distortion reflects the self-distortion in the model, which has approximately the same signal power as the TX leakage.

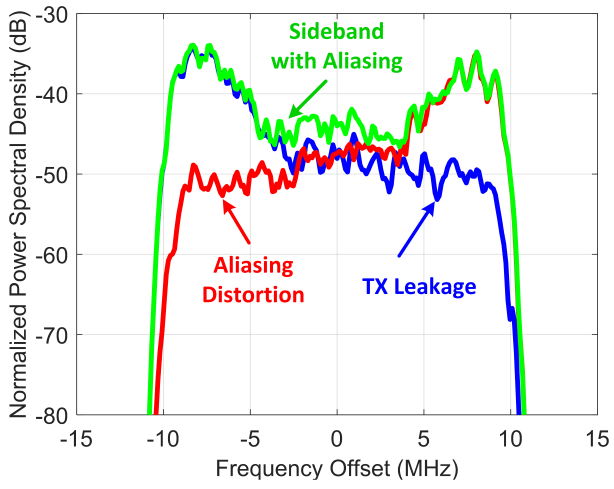

Fig. 18. The spectral demonstration of the mismatch and match cases in experiment.

In the low-rate condition, the model structure was modified and more cross-term products were selected. The number of the threshold value K was set 10, memory depth was 3, totally

resulting in 83 coefficients. Because some cross-terms have already been included in the memory model, only a moderate increase in the number of coefficients in this case. The baseband input signal was fed into the modified model to fit sideband with aliasing and TX leakage, respectively. According to the experimental results of the TX leakage suppression, the cross-term products are perceived to take care of the aliasing issue. In the experimental results, the suppression residual of the aliasing-distorted sideband in match case is around -60 dB as shown in Fig. 19. The suppression of TX leakage in mismatch case in Fig. 20 reaches the similar performance as that in the match case, suggesting that the strong aliasing-distortion has been effectively removed. Therefore, the excellent accuracy of suppression model at low sampling frequency for the TX leakage cancellation has been experimentally proved.

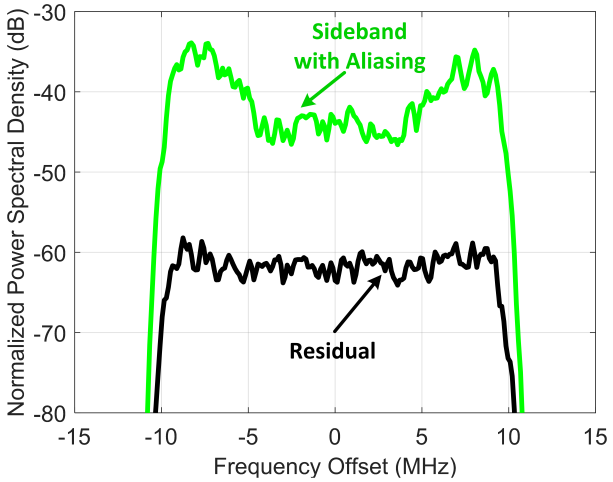

Fig. 19. The suppression performance of match case at low sampling rate.

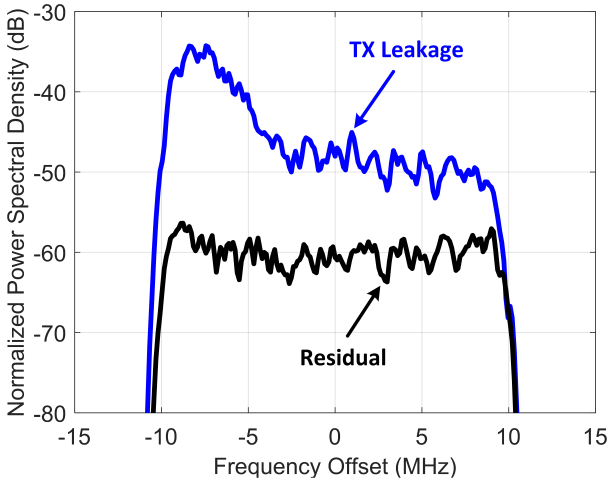

Fig. 20. The suppression performance of mismatch case at low sampling rate.

B. Model Accuracy Discussion

To have a better observation of the suppression model accuracy, more tests of TX leakage suppression with different

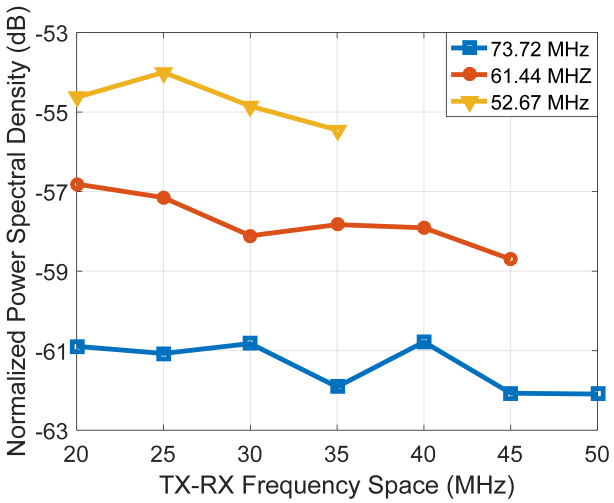

Fig. 21. Comparison of the normalized power spectral densities vs. TX-RX frequency spacings under different sampling rates.

system configuration were performed. Residual interference after suppression were evaluated against different TX-RX frequency spacings and different sampling rates, namely 73.72 MHz, 61.44 MHz and 52.67 MHz, which corresponded to 5, 6 and 7 times down-sampling, respectively.

When it comes to the TX-RX spacing, intuitively, a closer location of TX-RX carriers will make the suppression more challenging, as the leakage close to in-band signal is stronger. However, it has been found that as long as the sampling rate is chosen, the factor of TX-RX spacing has negligible influence on cancellation performance. For instance, at sampling rate of 61.44 MHz in Fig. 21, the residual of the TX leakage cancellation was around -58 dB, regardless of RX carrier locations. This result reflects the feasibility and flexibility of the DVR model over the Volterra-based models. Rather than configuring the nonlinear order according to the specific leakage locations, the DVR model utilizes the same nonlinear structure and achieves the fairly comparable suppression across the whole out-of-band frequency. Therefore, the proposed DVR model is much more flexible compared to the Volterra models.

It was noticed that the suppression performance is degraded with decreasing the sampling rate. This is caused by several reasons. Firstly, as mentioned in Section III, using cross-terms is only an approximation to interpolation. It cannot completely eliminate aliasing effect. Aliasing becomes more severe with lower sampling rate that leads to worse performance. Secondly, lower sampling rate results in lower correlation between data samples and noise floor also arises, that can cause model accuracy degradation. This performance degradation is relatively small. It was also noticed that the maximum achievable TX-RX frequency spacing is limited by the sampling rate. On one hand, with the reduction of sampling rate, the suppression performance is degraded, pulling up the residual level. On the other hand, the power of the sideband leakage drops with the increasing TX-RX spacing. Therefore, a point will be reached where the leakage is too weak to be effectively canceled under low sampling rate. This is the reason why the maximum TX-RX distance of the 52.67 MHz case is shorter than that of the

73.72 MHz case.

C. Hardware Implementation Comparison

To eliminate aliasing effect, more cross terms are needed to be added into the suppression model in the low sampling rate case, resulting in a larger number of coefficients required. It is true that the model implementation can be more complex compared to that used in the conventional high sampling approaches. However, the overall system complexity will be much lower because high order up-sampling can be avoided and fewer taps are required in the band-limiting filter. Furthermore, with the low sampling rate, the digital circuits can be operated at a low clock rate which can lead to significant reduction of power consumption of the circuits. In this section, we compare our approach with the solution proposed in [9], called the conventional approach, in terms of hardware resource utilization and power consumption to illustrate the benefits of the proposed solution.

For fair comparison, we set the same sampling rates for both solutions at the input and the final output, shown in Fig. 22. In the conventional approach [9], the input samples were interpolated by 6 times from 61.44 MSPS to the full-rate of 368.64 MSPS and then fed into the suppression model. The aliasing-free sideband replica was then generated and down-sampled to match the leakage data rate at the output. The block diagram of the model operation is shown in Fig. 22 (a). In the up-sampling operation, five consecutive zeros were inserted after every sample and then the signal was filtered by a low-pass FIR filter with 167 delay taps to smooth the waveform. The high sampling rate was kept during the nonlinear signal generation. The down-sampling process was implemented in combination with the band-limiting filtering, namely, rather than producing a 368.64 MSPS output, the band-limiting filter only generated one output sample every 6 clock cycles, reducing the sampling rate to 61.44 MSPS. By contrast, our proposed method used the same low sampling rate of 61.44 MSPS throughout the whole process, as shown in Fig. 22 (b). The conventional solution required 43 coefficients for the behavioral model to achieve the same cancellation performance as that achieved in the full-speed case, depicted in Fig. 17, while the proposed scheme used 83 coefficients and its performance is shown in Fig. 20. Because of a high sampling rate used, 125 delay taps were required for the band-limiting filter in the conventional approach while in the low sampling case, only 61 delay taps were needed.

Since most of hardware operations involve multiplications and additions [25], the hardware complexities can be estimated with the number of DSP48 units employed on Xilinx FPGA board (one DSP48 includes one multiplier and one adder). The detailed comparison of DSP48 resource utilization is listed in Table IV. Although the conventional approach only requires 29 DSPs for the nonlinear model construction, compared to 44 in the proposed approach, it requires many more DSP units to implement interpolation and band-limiting function because of the high data processing rate. Consequently, the total number of DSP units used in the conventional approach is almost doubled as that required in the proposed approach.

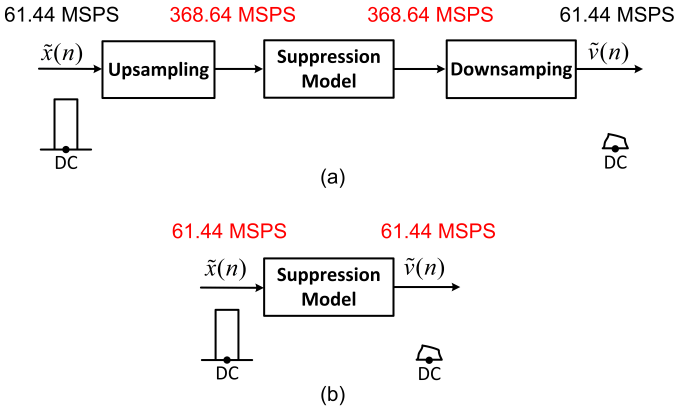

Fig. 22. The block diagrams of model operation: (a) the conventional approach and (b) the proposed approach.

Additionally, the clock speed can, to a great extent, affect the energy consumption of the entire system. In this work, we used Xilinx power estimator (XPE) [26], developed by Xilinx company, to approximate the power dissipation based on the data processing rate and the number of DSP48 units used. The power dissipated by the entire FPGA chip (on-chip power) and DSP units only (DSP slice power) are reported in Table V. Since there is 83.33% decease in the data processing rate in the proposed method compared to the conventional approach, 48.77% and 80.00% savings can be achieved for on-chip power and DSP slice power, respectively. From these results, we can see that, even though adding additional cross terms increases the model implementation complexity, the overall system complexity is still considerably lower and the power consumption of the system can be dramatically reduced because a much lower clock rate is required.

TABLE IV
HARDWARE COMPLEXITY COMPARISON

Block Function	DSP Units	
	Conventional	Proposed
Interpolation FIR Filter	56	0
Frequency Shift	3	3
Nonlinear Model	29	44
Band-limiting Filter	126	62
Total	214	109

TABLE V
POWER DISSIPATION COMPARISON

	Conventional		Proposed	Reduction
Processing Rate	368.64 MHz	61.44 MHz	61.44 MHz	83.33%
DSP Units	88	126	109	
On-chip Power	0.611 W		0.313 W	48.77%
DSP Slice Power	0.355 W		0.071 W	80.00%

VI. CONCLUSION

To alleviate receiver desensitization issue in FDD transceivers, a technique of suppressing TX-induced interference at low sampling rate has been proposed. The theoretical

analysis reveals that aliasing effect caused by the low sampling rate can be eliminated by adding cross-term products in the behavioral model and the experimental results have proved the effectiveness of the proposed approach. By employing the DVR model, it also shows that the same model structure can be used across the whole out-of-band frequencies regardless of the RX-TX spacing, which makes the model deployment very flexible. Because a low sampling rate is used, the implementation complexity and power consumption of the system can be significantly reduced by employing the proposed approach.

It is worth pointing out that, although the final model structure appears to be quite similar to that in the existing behavioral models, e.g., GMP/DVR models that are used for compensating memory effects induced by the PA, in this work, we showed, for the first time, that the aliasing effects in the sideband replica generation can be effectively eliminated by using cross-term products in the nonlinear model construction instead of using high sampling rate interpolation in the input signal. This provides an effective solution for reducing cost and in particular power consumption of digital signal processing in this application in future wideband systems.

APPENDIX
DERIVATION OF THE THIRD ORDER POLYNOMIAL INTERPOLATION TERMS

Assuming

$$\tilde{x}(2) = [\tilde{x}(1) + \tilde{x}(3)]/2, \tag{A.1}$$

we can have

$$|\tilde{x}(2)|^2 \tilde{x}(2) = \frac{|\tilde{x}(1) + \tilde{x}(3)|^2}{4} \times \frac{[\tilde{x}(1) + \tilde{x}(3)]}{2}. \tag{A.2}$$

If we define $\tilde{x}(1)$ and $\tilde{x}(3)$ as $\tilde{x}(1) = a + bj$, $\tilde{x}(3) = c + dj$, respectively, we thus can obtain

$$\begin{aligned} |\tilde{x}(1) + \tilde{x}(3)|^2 &= |a + c + (b + d)j|^2 \\ &= (a + c)^2 + (b + d)^2 \\ &= a^2 + b^2 + c^2 + d^2 + 2ac + 2bd \\ &= |\tilde{x}(1)|^2 + |\tilde{x}(3)|^2 + 2ac + 2bd. \end{aligned} \tag{A.3}$$

Note that $\tilde{x}(1)$ and $\tilde{x}(3)$ can also be represented as $\tilde{x}(1) = |\tilde{x}(1)|\, e^{j\theta_1}$ and $\tilde{x}(3) = |\tilde{x}(3)|\, e^{j\theta_3}$, respectively. If the corresponding real and imaginary part of $\tilde{x}$ is given by $\mathrm{Re}(\tilde{x}) = |\tilde{x}| \cos\theta$ and $\mathrm{Im}(\tilde{x}) = |\tilde{x}| \sin\theta$, respectively, (A.3) can then be re-written as

$$\begin{aligned} &|\tilde{x}(1)|^2 + |\tilde{x}(3)|^2 + 2ac + 2bd \\ &= |\tilde{x}(1)|^2 + |\tilde{x}(3)|^2 + 2\,|\tilde{x}(1)| \cos\theta_1\, |\tilde{x}(3)| \cos\theta_3 \\ &\quad + 2\,|\tilde{x}(1)| \sin\theta_1\, |\tilde{x}(3)| \sin\theta_3. \end{aligned} \tag{A.4}$$

Substituting the cosine term,

$$\cos(\theta_1 - \theta_3) = \cos\theta_1 \cos\theta_3 + \sin\theta_1 \sin\theta_3, \tag{A.5}$$

in (A.4), we obtain

$$\begin{aligned} &|\tilde{x}(1) + \tilde{x}(3)|^2 \\ &= |\tilde{x}(1)|^2 + |\tilde{x}(3)|^2 + 2ac + 2bd \\ &= |\tilde{x}(1)|^2 + |\tilde{x}(3)|^2 + 2\,|\tilde{x}(1)|\, |\tilde{x}(3)| \cos(\theta_1 - \theta_3). \end{aligned} \tag{A.6}$$

Finally, we have

$$\begin{aligned} |\tilde{x}(2)|^2 \tilde{x}(2) &= \frac{|\tilde{x}(1) + \tilde{x}(3)|^2}{4} \times \frac{[\tilde{x}(1) + \tilde{x}(3)]}{2} \\ &= \frac{|\tilde{x}(1) + \tilde{x}(3)|^2 \times \tilde{x}(1)}{8} + \frac{|\tilde{x}(1) + \tilde{x}(3)|^2 \times \tilde{x}(3)}{8} \\ &= \frac{[|\tilde{x}(1)|^2 + |\tilde{x}(3)|^2 + 2\,|\tilde{x}(1)|\, |\tilde{x}(3)| \cos(\theta_1 - \theta_3)] \times \tilde{x}(1)}{8} \\ &\quad + \frac{[|\tilde{x}(1)|^2 + |\tilde{x}(3)|^2 + 2\,|\tilde{x}(1)|\, |\tilde{x}(3)| \cos(\theta_1 - \theta_3)] \times \tilde{x}(3)}{8}. \end{aligned} \tag{A.7}$$

REFERENCES

[1] 3GPP Spec. LTE. (2016). Evolved Universal Terrestrial Radio Access (E-UTRA); User Equipment (UE) radio transmission and reception (3GPP TS 36.101 version 13.3.0 Release 13) May. 2016, [Online]. Available: http://www.etsi.org/standards-search.

[2] Z. Fu, L. Anttila, M. Abdelaziz, M. Valkama, and A. M. Wyglinski, "Frequency-selective digital predistortion for unwanted emission reduction," *IEEE Trans. Commun.*, vol. 63, no. 1, pp. 254–267, Jan. 2015.

[3] M. Abdelaziz, L. Anttila, J. R. Cavallaro, S. S. Bhattacharyya, A. Mohammadi, F. Ghannouchi, M. Juntti, and M. Valkama, "Low-complexity digital predistortion for reducing power amplifier spurious emissions in spectrally-agile flexible radio," in *2014 9th International Conference on Cognitive Radio Oriented Wireless Networks and Communications (CROWNCOM)*, Jun. 2014, pp. 323–328.

[4] C. Yu, M. Allegue-Martinez, Y. Guo, and A. Zhu, "Output-controllable partial inverse digital predistortion for RF power amplifiers," *IEEE Trans. Microw. Theory Tech.*, vol. 62, no. 11, pp. 2499–2510, Nov. 2014.

[5] J. Kim, P. Roblin, D. Chaillot, and Z. Xie, "A generalized architecture for the frequency-selective digital predistortion linearization technique," *IEEE Trans. Microw. Theory Tech.*, vol. 61, no. 1, pp. 596–605, Jan. 2013.

[6] S. A. Bassam, M. Helaoui, and F. M. Ghannouchi, "Channel-selective multi-cell digital predistorter for multi-carrier transmitters," *IEEE Trans. Commun.*, vol. 60, no. 8, pp. 2344–2352, Aug. 2012.

[7] P. Roblin, S. K. Myoung, D. Chaillot, Y. G. Kim, A. Fathimulla, J. Strahler, and S. Bibyk, "Frequency-selective predistortion linearization of RF power amplifiers," *IEEE Trans. Microw. Theory Tech.*, vol. 56, no. 1, pp. 65–76, Jan. 2008.

[8] T. O'Sullivan, R. A. York, B. Noren, and P. M. Asbeck, "Adaptive duplexer implemented using single-path and multipath feedforward techniques with BST phase shifters," *IEEE Trans. Microw. Theory Tech.*, vol. 53, no. 1, pp. 106–114, Jan. 2005.

[9] M. Omer, R. Rimini, P. Heidmann, and J. S. Kenney, "A compensation scheme to allow full duplex operation in the presence of highly nonlinear microwave components for 4G systems," in *IEEE MTT-S International Microwave Symposium Digest*, Jun. 2011, pp. 1–4.

[10] ——, "A PA-noise cancellation technique for next generation highly integrated RF front-ends," in *2012 IEEE Radio Frequency Integrated Circuits Symposium*, Jun. 2012, pp. 471–474.

[11] ——, "All digital compensation scheme for spur induced transmit self-jamming in multi-receiver RF frond-ends," in *IEEE/MTT-S International Microwave Symposium Digest*, Jun. 2012, pp. 1–3.

[12] A. Kiayani, L. Anttila, and M. Valkama, "Digital suppression of power amplifier spurious emissions at receiver band in FDD transceivers," *IEEE Signal Process. Lett.*, vol. 21, no. 1, pp. 69–73, Jan. 2014.

[13] A. Kiayani, M. Abdelaziz, L. Anttila, V. Lehtinen, and M. Valkama, "DSP-based suppression of spurious emissions at RX band in carrier aggregation FDD transceivers," in *2014 22nd European Signal Processing Conference (EUSIPCO)*, Sep. 2014, pp. 591–595.

[14] A. Kiayani, L. Anttila, and M. Valkama, "Modeling and dynamic cancellation of TX-RX leakage in FDD transceivers," in *2013 IEEE 56th International Midwest Symposium on Circuits and Systems (MWSCAS)*, Aug. 2013, pp. 1089–1094.

[15] C. Yu, W. Cao, Y. Guo, and A. Zhu, "Digital compensation for transmitter leakage in non-contiguous carrier aggregation applications with FPGA implementation," *IEEE Trans. Microw. Theory Tech.*, vol. 63, no. 12, pp. 4306–4318, Dec. 2015.

[16] C. Yu and A. Zhu, "Modeling and suppression of transmitter leakage in concurrent dual-band transceivers with carrier aggregation," in *2015 IEEE MTT-S International Microwave Symposium*, May 2015, pp. 1–3.

[17] S. Farsi, H. Gheidi, H. T. Dabag, P. S. Gudem, D. Schreurs, and P. M. Asbeck, "Modeling of deterministic output emissions of power amplifiers into adjacent receive bands," *IEEE Trans. Microw. Theory Tech.*, vol. 63, no. 4, pp. 1250–1262, Apr. 2015.

[18] A. Frotzscher and G. Fettweis, "Baseband analysis of Tx leakage in WCDMA zero-IF-receivers," in *2008 3rd International Symposium on Communications, Control and Signal Processing*, Mar. 2008, pp. 129–134.

[19] J. Kim and K. Konstantinou, "Digital predistortion of wideband signals based on power amplifier model with memory," *Electron. Lett.*, vol. 37, no. 23, pp. 1417–1418, Nov. 2001.

[20] D. R. Morgan, Z. Ma, J. Kim, M. G. Zierdt, and J. Pastalan, "A generalized memory polynomial model for digital predistortion of RF power amplifiers," *IEEE Trans. Signal Process.*, vol. 54, no. 10, pp. 3852–3860, Oct. 2006.

[21] A. Zhu, J. C. Pedro, and T. J. Brazil, "Dynamic deviation reduction-based volterra behavioral modeling of RF power amplifiers," *IEEE Trans. Microw. Theory Tech.*, vol. 54, no. 12, pp. 4323–4332, Dec. 2006.

[22] C. Yu, L. Guan, E. Zhu, and A. Zhu, "Band-limited volterra series-based digital predistortion for wideband RF power amplifiers," *IEEE Trans. Microw. Theory Tech.*, vol. 60, no. 12, pp. 4198–4208, Dec. 2012.

[23] A. Zhu, "Decomposed vector rotation-based behavioral modeling for digital predistortion of RF power amplifiers," *IEEE Trans. Microw. Theory Tech.*, vol. 63, no. 2, pp. 737–744, Feb. 2015.

[24] M. Y. Cheong, S. Werner, J. E. Cousseau, and R. Wichman, "Spectral characteristics of a piecewise linear function in modeling power amplifier type nonlinearities," in *21st Annual IEEE International Symposium on Personal, Indoor and Mobile Radio Communications*, Sep. 2010, pp. 639–644.

[25] W. Cao and A. Zhu, "A modified decomposed vector rotation-based behavioral model with efficient hardware implementation for digital predistortion of RF power amplifiers," *IEEE Trans. Microw. Theory Tech.*, vol. 65, no. 7, pp. 2443–2452, Jul. 2017.

[26] Xilinx All Programmable. (2017). Xilinx Power Estimator User Guide, [Online]. Available: https : / / www . xilinx . com / support / documentation / sw_manuals / xilinx2014_1 / ug440 - xilinx - power - estimator.pdf.

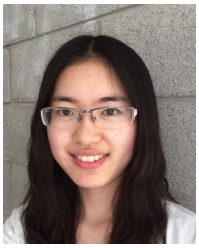

Wenhui Cao (S'15) received the B.E. degree in automation from Beijing University of Chemical Technology, Beijing, China, in 2013 and Ph.D. degree in electronic engineering from University College Dublin (UCD), Dublin, Ireland, in 2017.

She was with the RF and Microwave Research Group at UCD from 2013 to 2017 and now she is a Lecturer in the School of Electronics and Information at Hangzhou Dianzi University, Hangzhou, China. Her research interests include nonlinear behavioral modeling and linearization of RF power amplifiers, digital post-correction of high speed ADCs, and digital suppression of TX-induced interference in FDD transceiver. She also has interests in high performance field-programmable gate-array (FPGA) implementation methodologies.

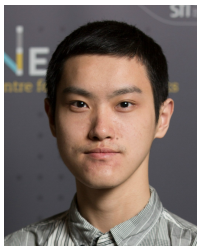

Yue Li Yue Li (S'17) received the B.E. degree in information engineering from Southeast University, Nanjing, China, in 2016. He is currently working towards the Ph.D. degree at University College Dublin, Dublin, Ireland.

He is currently with the RF and Microwave Research Group, UCD. His current research interests include behavioral modeling and digital predistortion for RF power amplifiers.

Anding Zhu (S'00-M'04-SM'12) received the B.E. degree in telecommunication engineering from North China Electric Power University, Baoding, China, in 1997, the M.E. degree in computer applications from Beijing University of Posts and Telecommunications, Beijing, China, in 2000, and the Ph.D. degree in electronic engineering from University College Dublin (UCD), Dublin, Ireland, in 2004.

He is currently a Professor with the School of Electrical and Electronic Engineering, UCD. His research interests include high-frequency nonlinear system modeling and device characterization techniques with a particular emphasis on behavioral modeling and linearization of RF power amplifiers for wireless communications. He also has interests in high efficiency power amplifier design, wireless transmitter architectures, digital signal processing and nonlinear system identification algorithms.